# 5 DMFT for Moiré Systems

Tim Wehling
Universität Hamburg
Notkestraße 9-11, 22607 Hamburg

## Contents



E. Pavarini, E. Koch, A. Lichtenstein, and D. Vollhardt (eds.)
Understanding Correlated Materials with DMFT
Modeling and Simulation Vol. 15
Forschungszentrum Jülich, 2025, ISBN 978-3-95806-813-1
http://www.cond-mat.de/events/correl25

# 1 Strong correlations and superconductivity in moiré systems

Two-dimensional (2D) materials are crystalline solids consisting of a single or a few layers of atoms arranged in a flat, planar structure [1, 2]. Unlike conventional three-dimensional materials, which extend in all spatial directions, 2D materials are confined to just two dimensions. The most well-known example is graphene, a single layer of carbon atoms arranged in a honeycomb lattice. Graphene sparked strong interest for its mere existence as a 2D crystal seemingly violating the Mermin Wagner theorem and from early on also for its special electronic properties with low-energy electronic quasiparticles behaving like massless Dirac fermions [3, 4].

Since then, a wide family of 2D materials has been explored, including transition metal dichalcogenides (TMDs), hexagonal boron nitride (h-BN), and phosphorene, realizing a variety of atomically thin systems including metals, semimetals, semiconductors, insulators, superconductors, topological insulators etc. An especially exciting development in the field of 2D materials is the controlled stacking of different monolayers, which enables the creation of van der Waals heterostructures—artificial materials formed by layering 2D crystals without the constraints of lattice matching [1, 2].

When two layers with slightly mismatched lattice constants or a small twist angle $\theta$ between them are stacked, they produce a moiré pattern — a long-wavelength modulation pattern — resulting from the superposition of the two atomic lattices as can be seen from Fig.1. The moiré periodicity can significantly modify the electronic properties of the system by acting as a periodic potential or as a periodically modulated interlayer tunneling at the emergent length scale defined by the moiré lattice.

In particular, twisted bilayer graphene (TBG) near the so-called "magic angle" ($\sim 1.1^\circ$) hosts flat topological electronic bands, which dramatically enhance electron-electron interactions, leading to correlated insulating states and even superconductivity [5–7]. Similar moiré-induced correlation phenomena have since also been observed in heterostructures based on TMDs [8–11], establishing moiré engineering as a versatile platform for exploring strongly correlated and topological phases of matter [7, 12, 13].

The enhancement of correlation effects in moiré structures can be rationalized from the follow-

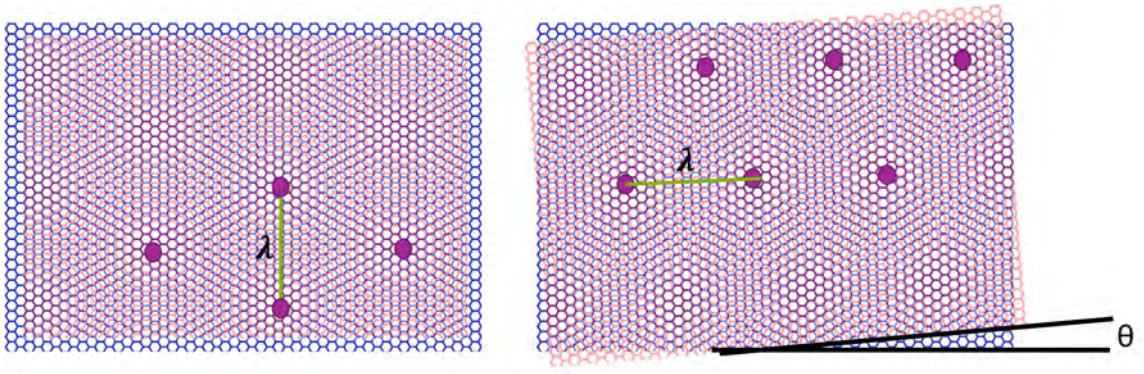


**Fig. 1:** *Moiré superlattices in van der Waals heterostructures from lattice mismatch (left) and twisting (right) of the 2D constituent layers.*

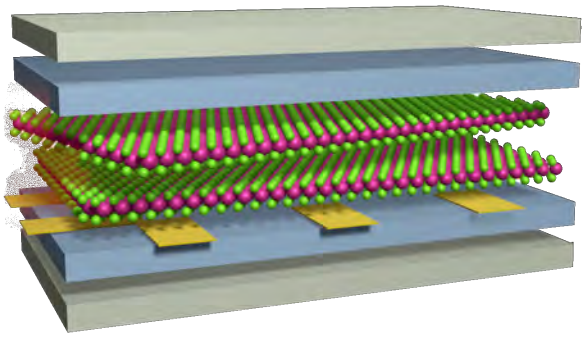

**Fig. 2:** *Typical experimental setup to realize and probe electronic correlation phenomena in moiré systems: a twisted 2D bilayer giving rise to the actual moiré structure is sandwiched between dielectric spacer layers, often hBN (blue), and outer gate electrodes (gray). The gate electrodes allow to apply vertical electric fields and to dope the sample via the field effect. The dielectric environment controls the effective strength of Coulomb interactions in the active 2D moiré bilayer.*

ing argument. The moiré periodicity is associated the characteristic length scale of the moiré lattice constant $\lambda$. For twisted bilayers of the same material, the length scale $\lambda$ follows from the twist angle $\theta$ and the original lattice constant $a$ according to

$$\lambda(\theta) = a/(2\sin(\theta/2)) \approx a/\theta,$$

where the latter relation holds at small twist angles. Assuming now a parabolic dispersion for the electrons, we arrive at the following scaling of the band width $W$ and the Coulomb interaction $U$ with twist angle

$$\left.\begin{aligned} W &\sim \frac{\hbar^2}{2m}\frac{1}{\lambda^2} \propto \theta^2 \\ U &\sim \frac{e^2}{\kappa}\frac{1}{\lambda} \propto \theta \end{aligned}\right\} \Rightarrow \frac{U}{W} \propto \frac{1}{\theta}\,. \tag{1}$$

Typical experiments on electron correlations in 2D material moiré structures are based on setups as depicted in Fig. 1, which lead to a quite remarkable tunability in comparison to conventional bulk systems: tuning twist angle and the dielectric environment ($\kappa$ in Eq. (1)) allows to control the relative strength of electron correlations in the moiré system, while the gate voltages allow for wide tuning of the filling and reshaping of band structures as we will see.

In this chapter, we give an overview of correlated electron physics in moiré systems, starting with a selection of experimental observations of strong correlation effects and superconductivity in van der Waals based moiré systems. Afterwards we will turn towards the theoretical description of these phenomena focusing on moiré band structures and the modeling of correlation effects in these in graphene and TMD based moiré systems.

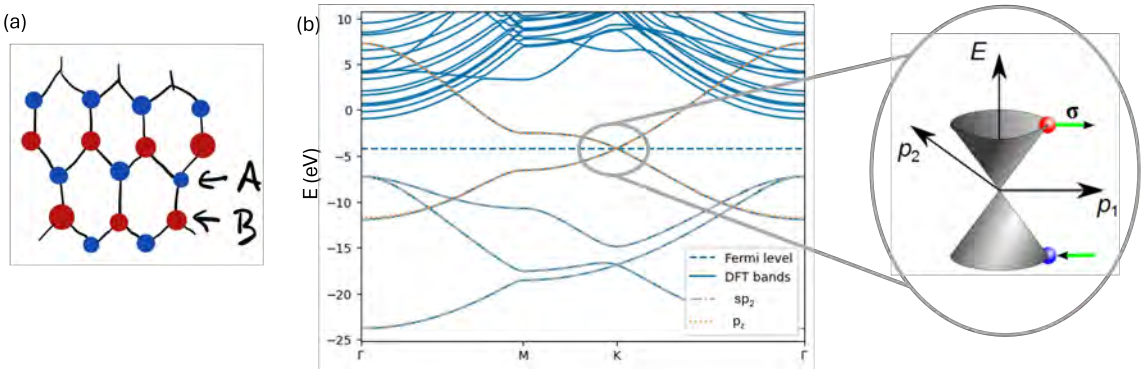


**Fig. 3:** *Crystal structure (a) and electronic band structure with close up view around the Fermi level of monolayer graphene (b). The low-energy electronic states are described by a Dirac equation with inherent pseudospin degree of freedom resulting from the two-sublattice structure of graphene (see sublattices A and B marked in panel a). The nodal points in the band structure are referred to as Dirac points. Electrons acquire a Berry phase of $\pm\pi$ upon encircling the Dirac points at K (K').*

## 1.1 Graphene-based moiré materials

The band structure of monolayer graphene is shown in Fig. 3. The bands around the Fermi level are made up from Carbon $p_z$ orbitals and exhibit a bandwidth of more than $10$ eV. The low-energy quasiparticles are near the Brillouin zone corners $\pm K = K, K'$ and described by a Dirac Hamiltonian: $H_D = \hbar v_f \mathbf{k} \cdot \boldsymbol{\sigma}$, where $v_f$ is the Fermi velocity, $\mathbf{k}$ is the crystal momentum and $\boldsymbol{\sigma} = (\sigma_x, \pm\sigma_y)$ is a vector of Pauli matrices. Here, the Pauli matrices refer to a pseudospin describing the sublattice degree of freedom in graphene, i.e., the degree of freedom for electrons to reside in honeycomb sublattice A or B. The Brillouin zone regions around $K$ and $K'$ are called "valleys" and the corresponding band degeneracy points are called Dirac points. The pseudospin of the electrons rotates in the $x$-$y$-plane and the wave function picks up a Berry phase of $\pm\pi$, when encircling the Dirac points at $\pm K$ in momentum space. This Berry phase will turn out to bestow bands in twisted bilayer graphene with a distinct topology that needs to be accounted for properly modeling of the correlated electron physics.

The strength of Mott-Hubbard type correlations in pure monolayer graphene has been assessed on the basis of interaction parameters derived from the constrained Random Phase Approximation (cRPA) [14, 15]. While the local Hubbard repulsion in free standing graphene reaches the scale of the band width, it turns out that screening by sizeable non-local interaction terms quenches Mott Hubbard correlations leading to a ratio of effective interaction to hopping $\tilde{U}/t \approx 1.6$ [15], which far below the value for the Mott transition on the honeycomb lattice $U^{\mathrm{Mott}}/t \approx 8$ and also smaller than the value of $U^{\mathrm{AMF}}/t \approx 3.5$ for the transition into a sublattice antiferromagnet. Taken together, charge neutral monolayer graphene is thus a Dirac material with characteristic Berry phase imprinted to the dispersion relation featuring weak electron correlations in the Mott Hubbard sense.

This situation changes drastically, when two graphene layers are stacked on top of each other with a twist angle on the order of $1.1^\circ$ —referred to as the "magic angle". A representative dop-

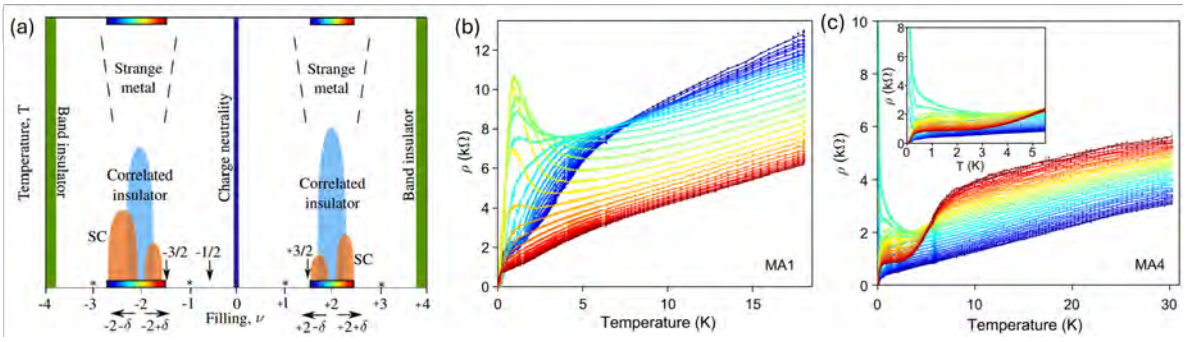


**Fig. 4:** *Phase diagram of near magic angle TBG as derived from transport experiments of Ref [16]. (a) Schematic phase diagram for magic angle TBG as a function of temperature and filling $\nu$ exhibiting superconducting regions (orange), correlated insulating states (light blue) and strange metal behavior with T-linear resistivity. (b,c) Experimentally measured resistivity ($\rho$) measured on two different TBG devices ("MA1", "MA4") with twist angles of $\theta = 1.16°$ and $1.18°$, respectively, as function of temperature for different fillings close to $\nu = \pm 2$ illustrate the manifestation of the strange metal, correlated insulating and superconducting states in electronic transport. The horizontal color bars in the left and right panel of the phase diagrams in (a) correspond to the transport data shown (b) and (c), respectively. Adapted from Ref. [16].*

ing and temperature dependent phase diagram is shown in Fig. 4. It is derived from transport experiments of Ref. [16] and is qualitatively in line with several other studies [5–7, 12, 17–20]. At low temperatures highly resistive states ("correlated insulators") emerge next to superconducting states—both of which are absent in the monolayer constituents. Close to the correlated insulators, there is a region featuring unusual transport behavior including linear-in-temperature resistivity referred to as strange metal phase. This phase diagram is indeed quite similar to cuprates and other correlated electron systems.

A large body of theoretical and experimental work has been ongoing to understand the electronic phase diagram of TBG. Taking together experiments like Refs. [5,6,16–22] the following overarching picture can drawn:

- Superconductivity emerges on the scale of roughly 1 K in certain filling ranges.
- Correlated insulating states occur at some integer fillings.
- The doping regions where superconductivity occurs and the integer fillings where the insulating states occurs are sample dependent.
- There is a temperature controlled fade out of insulating behavior (at integer $\nu$) and an onset of incoherent metallic behavior (for wider filling ranges) around 5–20 K.
- Different kinds of spontaneous symmetry breaking such as orbital ferromagnets or intervalley coherent states with characteristic sublattice interference patterns occur below characteristic temperatures on the order of 5 K.

TBG is indeed only one representative of a larger family of graphene-based multilayer moiré systems featuring similar correlation effects and (enhanced) superconductivity [23].

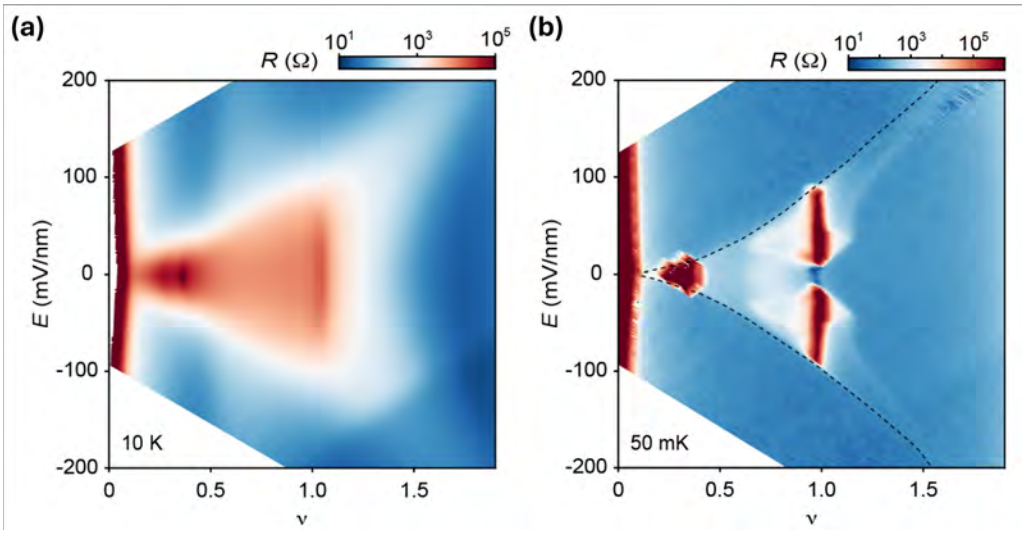


**Fig. 5:** *Emergent electronic phases in $tWSe_2$ as manifesting in transport experiments of Ref. [10]. The moiré band structure of the system is tunable by vertical displacement fields $E$. The longitudinal resistance $R$ of $tWSe_2$ at twist angle $3.65°$ is shown as a function of displacement field $E$ and filling $\nu$ at 10 K (a) and 50 mK (b). From Y. Xia, Z. Han, K. Watanabe, T. Taniguchi, J. Shan, and K. F. Mak: Unconventional Superconductivity in Twisted Bilayer $WSe_2$, arXiv:2405.14784. Copyrighted under CC BY-NC-ND 4.0.*

We will discuss in section 2.2 how interference of electronic states from the different bilayers modulated by the moiré pattern of TBG can lead to flat bands with extremely narrow bandwidths, where the kinetic energy of charge carriers is strongly suppressed thereby promoting electronic correlation effects. We will also work out how modeling of these correlation effects can be achieved focusing in particular on studies employing dynamical mean-field theory.

## 1.2 Transition metal dichalcogenide moiré systems

The emergence of 2D moiré superlattices in van der Waals stacks is very general and not limited to graphene-based systems. Correspondingly, moiré flat band physics has been explored in multiple platforms particularly TMDs [8–13].

In their monolayer form TMDs $MX_2$ with M$\in \{\mathrm{Mo}, \mathrm{W}\}$ and X$\in \{\mathrm{S}, \mathrm{Se}\}$ are semiconductors with quasi particle band gaps on the order of eV. These materials are structurally similar to graphene by also having honeycomb lattice structures, where now one sublattice is filled by the metal atoms M and the other sublattice by the chalcogens $X$ (c.f. Fig. 12). The moiré physics emerges here upon building multilayer structures with a lattice mismatch (heterobilayers) or twist angle (hetero- and homobilayers). Several correlated states including correlated insulators [8,24,25] featuring rich multi-orbital physics [26] and quantum critical behavior [27,28] as well as topological Kondo physics [29] have been reported. Early experiments on $5.0°$ twisted $WSe_2$ hinted at the existence of superconducting phases in moiré TMDs [8] but the situation remained controversial. Recent experiments on $3.65°$ [10] and $5.1°$ [11] twisted bilayer $WSe_2$ ($tWSe_2$) reported evidence for superconductivity, albeit at significantly lower critical temperatures than [8].

We illustrate in Fig. 5 the resistivity of twisted bilayer $WSe_2$ at twist angle $3.65^\circ$ [10] measured as function of doping and displacement field for two different temperatures, 10 K and 50 mK. At 10 K, there is a strong asymmetry of the resistivity around $\nu = 1$ and particularly enhanced scattering right at $\nu = 1$. Lowering the temperature to 50 mK, one sees, highly resistive insulating states at $\nu = 1$ for a certain region of displacement fields and a low-resistance metallic state in between. Right at the boundary of the metallic and the insulating states near $\nu = 1$, a zero resistance superconducting states occurs. Again, as in the 10 K, there is a strong doping asymmetry around $\nu = 1$. Transitions between all these different phases are tunable by doping $\nu$, vertical displacement field $E_z$ and additionally temperature.

# 2 Model building for moiré systems: From moiré band structures to correlated electron lattice models

In this section, we will exemplify the quenching of kinetic energy and formation of flat bands in moiré systems with three examples: (i) In $MoS_2$, $WS_2$ and $MoSe_2$ twisted bilayers Mott Hubbard correlations and spin fluctuations emerge in the $\Gamma$ valley. This case is particularly simple and illustrates most clearly how, spatially modulated potentials and interlayer hybridization quench kinetic energy and give way to strong electron correlations in systems of formerly weakly correlated semiconducting constituents. Afterwards, we will turn towards the experimentally particularly relevant cases of twisted bilayer graphene (ii) and twisted $WSe_2$ bilayers, where moiré minibands stemming from the K and K' valley, carry distinct Berry curvature, leading to an interplay of electron correlations and topology. Along with these example cases we illustrate model building and practical implementations of dynamical mean-field based simulations of correlation effects.

## 2.1 Γ valley twisted TMD moiré bilayers

For moiré superlattices from semiconducting or semimetallic constituents, the emergent electronic states can be effectively described by continuum model Hamiltonians, in which the exact commensurability between the moiré pattern and the underlying atomic lattice is not essential. In bulk $WS_2$, $MoS_2$ and $MoSe_2$ and also corresponding non-twisted bilayers, the valence band maximum is located at the $\Gamma$ point and composed of layer-antibonding states that are separated from other states by hundreds of meV. This motivates the following one-band continuum model [30]

$$H = -\frac{\hbar^2 k^2}{2m^*} + V_{\mathrm{M}}(\mathbf{r}), \tag{2}$$

where $m^*$ is the effective mass and $V_{\mathrm{M}}(\mathbf{r})$ is the moiré potential felt by the holes near the valence band maximum at $\Gamma$. A standard way to obtain an estimate of the moiré potential is to assess which contributions to $V_{\mathrm{M}}(\mathbf{r})$ would be allowed by the system's symmetry and fit these contributions then to ab initio calculations.

The analysis of Ref. [30] shows that the twisted TMD homobilayers impose the dihedral symmetry $D_6$ on $V_{\mathrm{M}}(\mathbf{r})$. Time-reversal symmetry implies that $V_{\mathrm{M}}(\mathbf{r})$ must be real. Finally, $V_{\mathrm{M}}(\mathbf{r})$ is periodic with the moiré superlattice, which motivates the following plane-wave expansion

$$V_{\mathrm{M}}(\mathbf{r}) = \sum_{s=1}^{3} \sum_{j=1}^{6} V^s \mathrm{e}^{i(\mathbf{g}_j^s \cdot \mathbf{r} + \phi^s)}. \tag{3}$$

Here, $s$ is the $s$-th shell of six moiré reciprocal lattice vectors $\mathbf{g}_j^s = \mathcal{R}_{(j-1)\pi/3}\mathbf{G}^s$ ($j = 1, \ldots, 6$) with $\mathcal{R}_\alpha$ being the two-dimensional (2D) rotation matrix about an angle $\alpha$. The phase factors $\phi^s$ are constrained by symmetry to be either 0 or $\pi$. As shown in Ref. [30], the potential $V_{\mathrm{M}}(\mathbf{r})$ is well-captured by the three leading Fourier components. Thus, the Hamiltonian describing twisted TMDs is indeed a "real material" implementation of the textbook problem of nearly free electrons in a periodic potential.

The $D_6$ symmetry together with the moiré periodicity further demands that the high symmetry Wyckoff positions corresponding to the regions with AA stacking or regions with AB/BA stacking are extrema of the potential $V_{\mathrm{M}}(\mathbf{r})$. The DFT calculations of Ref. [30] show that the valence band maximum in the Bernal stacked regions (AB, BA) is higher in energy than in the AA regions. The low-energy moiré bands in $\Gamma$-valley TMD homobilayers are therefore generated by orbitals sitting on the honeycomb lattice formed by the AB/BA regions and $\Gamma$-valley TMDs homobilayers can be viewed as a moiré pendant of graphene.

The moiré lattice translation symmetry implies that Bloch's theorem applies on the moiré scale with moiré crystal momentum, $\mathbf{k}$, being a good quantum number. The single particle Hamiltonian from Eq. (2) is thus diagonal in $\mathbf{k}$ and takes the following form in the basis of plane waves $|\mathbf{k}+\mathbf{G}\rangle$

$$\langle \mathbf{k}+\mathbf{G}| \, H \, |\mathbf{k}+\mathbf{G}'\rangle = -\frac{\hbar^2|\mathbf{k}+\mathbf{G}|^2}{2m^*}\delta_{\mathbf{G},\mathbf{G}'} + V_{\mathrm{M}}(\mathbf{G}-\mathbf{G}'). \tag{4}$$

Here, $\mathbf{G}$ denotes vectors from the moiré reciprocal lattice, respectively and $V_{\mathrm{M}}(\mathbf{G}-\mathbf{G}')$ is the Fourier transform of $V_{\mathrm{M}}(\mathbf{r})$. Diagonalization of the Hamiltonian from Eq. (4) yields the plane-wave expansion coefficients $c^\alpha_{\mathbf{kG}}$ of the eigenstates

$$|\Phi^\alpha_{\mathbf{k}}\rangle = \sum_{\mathbf{G}} c^\alpha_{\mathbf{kG}} \, |\mathbf{k}+\mathbf{G}\rangle \, , \tag{5}$$

where $\alpha$ is the band index. These eigenstates are expanded up to a plane-wave cutoff $G_{\mathrm{c}}$, which depends in practice on the twist angle $\theta$. This "program" to deal with the moiré minibands is analogous to plane wave expansions of Bloch states in conventional solids.

In Fig. 6 we show the band structures for $\Gamma$-valley twisted TMDCs at twist angles in the range $1^\circ < \theta < 5^\circ$. The zero energy is defined as the top of the valence band. For this twist angle range it turns out to be sufficient to use $G_c = 4$–$5\, G^{\mathrm{M}}$, where $G^{\mathrm{M}} = |\mathbf{G}^{\mathrm{M}}_{1,2}|$, i.e., the solving the continuum models is numerically rather "light-weight".

From the valence band edge, two flat bands emerge which touch at Dirac points in the corners of the moiré Brillouin zone. We refer to these bands as "flat Dirac bands". Their shape is very similar in shape to the dispersion of graphene albeit at a completely different energy scale.

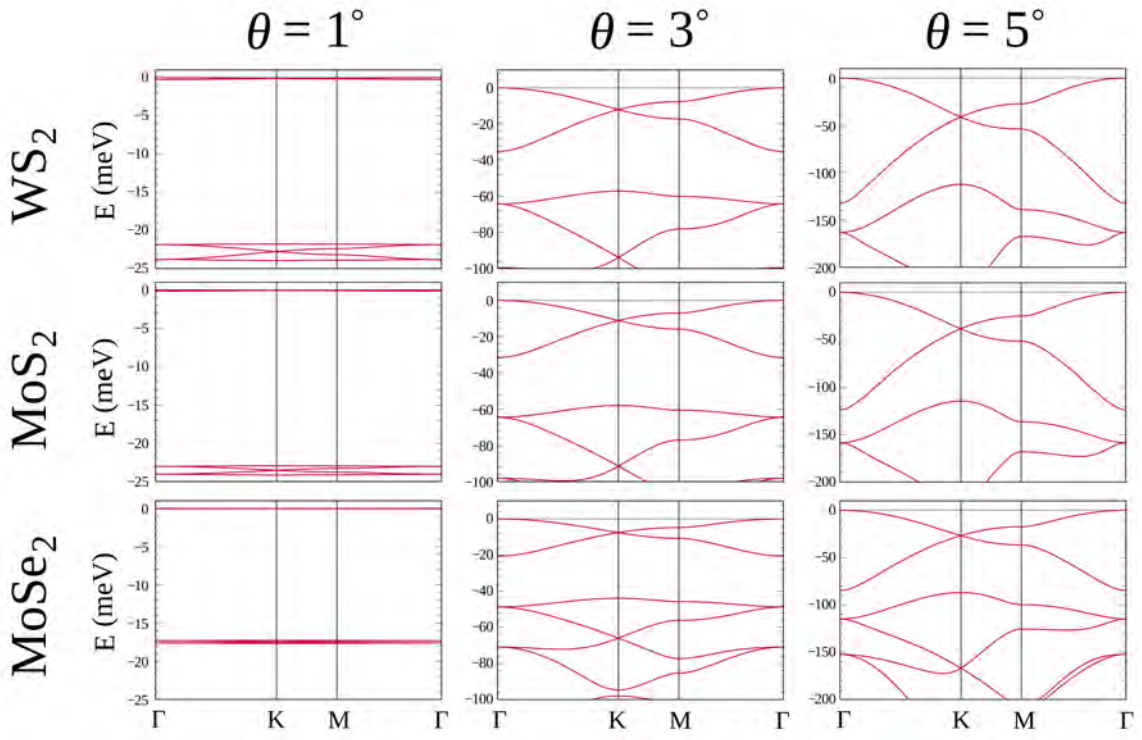


**Fig. 6:** *Band structures for the $\Gamma$-valley twisted TMDCs, $WS_2$ (top row), $MoS_2$ (middle row), and $MoSe_2$ (bottom row). We show the low-energy band evolution for the twist angle range $1^\circ < \theta < 5^\circ$. From Ref. [32].*

This is well understandable from the honeycomb form of the moiré potential, which resembles graphene. The flat Dirac bands are well isolated from other higher energy bands for $\theta < 5^\circ$ and their bandwidth increases approximately quadratically with the twist angle.

A decisive step in the model building for the treatment of strong electron correlations, is the formulation of lattice models describing the low-energy electronic degrees of freedom. For the case at hand, a Wannierization procedure analogously to conventional bulk systems is expedient. Based on our observations we construct a Wannier Hamiltonian for the isolated flat Dirac bands via projection [31] with one orbital per site for each moiré sublattice [32], where the AB and BA regions of the moiré play the role of the A and B sublattice sites in a honeycomb lattice.

We proceed, thus, with trial orbitals $|g^m\rangle$ (e.g. Gaussian orbitals) centered on sublattice sites $m \in \{\mathrm{A}, \mathrm{B}\}$ of the unit cell at the origin in real space, which are then projected onto the space spanned by the low energy Dirac bands to yield new states

$$|\phi^m_{\mathbf{k}}\rangle = \sum_\alpha |\Phi^\alpha_{\mathbf{k}}\rangle \langle \Phi^\alpha_{\mathbf{k}}|g^m\rangle \,. \tag{6}$$

By this step, we arrive at states $|\phi^m_{\mathbf{k}}\rangle$ spanning the space of the flat Dirac bands with a smooth gauge in $\mathbf{k}$-space. However, $\{|\phi^m_{\mathbf{k}}\rangle\}$ are not necessarily orthonormal. Using the projection matrix $P^{\alpha m}_{\mathbf{k}} = \langle \Phi^\alpha_{\mathbf{k}}|g^m\rangle$ we obtain the overlap matrix

$$S^{mn}_{\mathbf{k}} = \langle \phi^m_{\mathbf{k}}|\phi^n_{\mathbf{k}}\rangle = \left(P^\dagger_{\mathbf{k}} P_{\mathbf{k}}\right)^{mn} , \tag{7}$$

which is finally used to calculate the orthonormalized smooth gauge Bloch states via Löwdin orthonormalization at every $\boldsymbol{k}$

$$|\tilde{\psi}_{m\boldsymbol{k}}\rangle = \sum_{n\in\{A,B\}} |\phi_{n\boldsymbol{k}}\rangle \left(S^{-1/2}(\boldsymbol{k})\right)_{nm} . \tag{8}$$

Since the $|\tilde{\psi}_{m\boldsymbol{k}}\rangle$ exhibit a smooth gauge in $\boldsymbol{k}$-space, a Fourier transformation yields finally the desired Wannier functions in real space. The the $m^{\text{th}}$ Wannier function in unit cell $\boldsymbol{R}$ reads

$$|\boldsymbol{R}m\rangle = \frac{A_M}{(2\pi)^2} \int_{mBZ} d\boldsymbol{k}\, e^{-i\boldsymbol{k}\cdot\boldsymbol{R}} |\tilde{\psi}_{m\boldsymbol{k}}\rangle , \tag{9}$$

with $A_M$ being the moiré unit cell area and the integral running over the moiré Brillouin zone. Taking matrix elements of the original continuum model Hamiltonian $H$, Eqs. (2)–(4), w.r.t. the Wannier functions, yield the hopping and on-site matrix elements of a tight-binding description of the moiré band structure:

$$h_{\boldsymbol{R}n,\boldsymbol{R}'m} = \langle \boldsymbol{R}n|H|\boldsymbol{R}'m\rangle . \tag{10}$$

The following steps need to be implemented for actual calculations as, e.g., detailed in the supplement of Ref. [32]:

- Choose localized projector orbitals and obtain their plane-wave expansion:

$$|g^m\rangle = g^m_{\mathbf{k},\mathbf{G}} \,|\mathbf{k}{+}\mathbf{G}\rangle .$$

- Obtain plane wave expansion coefficients $c^\alpha_{\mathbf{kG}}$ of the eigenstates of the continuum model from diagonalization of the continuum model, Eq. (4), in $\mathbf{k}$-space:

$$|\Phi^\alpha_{\mathbf{k}}\rangle = \sum_{\mathbf{G}} c^\alpha_{\mathbf{kG}} \,|\mathbf{k}{+}\mathbf{G}\rangle .$$

- Calculate projector matrix for each $\mathbf{k}$:

$$P^{\alpha m}_{\mathbf{k}} = \langle \Phi^\alpha_{\mathbf{k}}|g^m\rangle = \sum_{\mathbf{G}} (c^\alpha_{\mathbf{kG}})^\dagger g^m_{\mathbf{kG}}.$$

- Calculate plane-wave expansion coefficients of the smooth gauge states $|\phi^m_{\mathbf{k}}\rangle = \sum_{\mathbf{G}} \phi^m_{\mathbf{kG}} \,|\mathbf{k}{+}\mathbf{G}\rangle$:

$$\phi^m_{\mathbf{kG}} = \sum_\alpha c^\alpha_{\mathbf{kG}} P^{\alpha m}_{\mathbf{k}} .$$

- Calculate overlap matrix $(S_{\mathbf{k}})^{nm}$ via Eq. (7).

- Calculate the plane-wave expansion coefficients of the orthonormalized smooth gauge Bloch states $|\tilde{\Phi}^m_{\mathbf{k}}\rangle = \sum_{\mathbf{G}} \tilde{c}^m_{\mathbf{kG}} \,|\mathbf{k}{+}\mathbf{G}\rangle$:

$$\tilde{c}^m_{\mathbf{kG}} = \sum_n \phi^n_{\mathbf{kG}} \cdot \left(S^{-1/2}_{\mathbf{k}}\right)^{nm} .$$

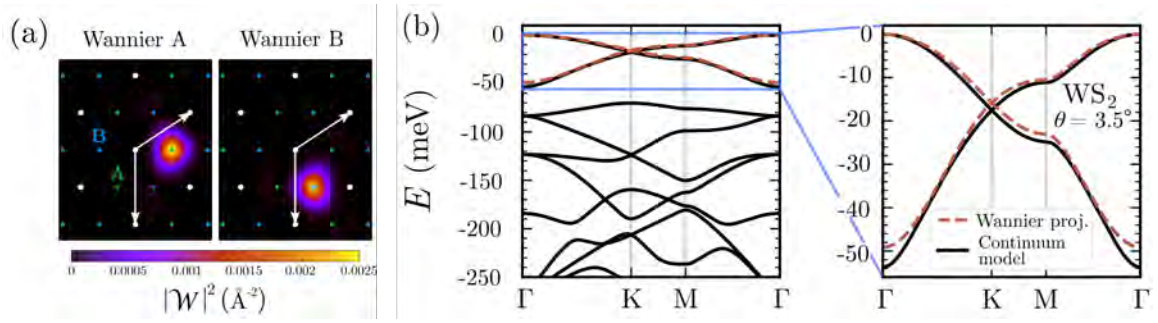


**Fig. 7:** *Wannier tight-binding model for twisted $WS_2$ at 3.5°. (a) Probability densities $|\mathcal{W}_m(\mathbf{r})|^2$ for Wannier orbitals centered in the sublattices A (green dots) and B (blue dots). White dots denote the Bravais lattice $\mathbf{R}$ and white arrows are the moiré lattice vectors. (b) Band structure of twisted bilayer $WS_2$ at the twist angle of $\theta = 3.5°$ from the continuum model (black solid line) and from the Wannier tight-binding model (red dashed line) of the two highest valence bands, where the hopping has been truncated after the third-nearest-neighbor terms. The right panel shows a zoom to the flat Dirac bands. From Ref. [32]*

- Obtain Wannier functions in real space:

$$\mathcal{W}_{\mathbf{R}m}(\mathbf{r}) = \langle \mathbf{r}|\tilde{\Phi}^m_{\mathbf{k}}\rangle = \frac{1}{N_{\mathbf{k}}\sqrt{A_{\mathrm{M}}}} \sum_{\mathbf{k}} \sum_{\mathbf{G}} \tilde{c}^m_{\mathbf{kG}} \mathrm{e}^{i\mathbf{K}\cdot(\mathbf{r}-\mathbf{R})} \ ,$$

  where the Brillouin zone integral from Eq. (9) is discretized with $N_{\mathbf{k}}$ points sampling the moiré Brillouin zone.

- Calculate Hamiltonian in Wannier basis by projecting the continuum Hamiltonian onto the orthonormalized smooth gauge Bloch states $|\tilde{\Phi}^m\rangle$:

$$\tilde{H}^{mn}_{\mathbf{k}} = \langle \tilde{\Phi}^m_{\mathbf{k}}|H|\tilde{\Phi}^n_{\mathbf{k}}\rangle \equiv \sum_{\mathbf{G},\mathbf{G}'} \left(\tilde{c}^m_{\mathbf{kG}}\right)^\dagger H_{\mathbf{kGG}'}\, \tilde{c}^n_{\mathbf{kG}'},$$

  where $H_{\mathbf{kGG}'}$ are the matrix elements of the Hamiltonian in Eq. (4).

- Fourier transform $\tilde{H}^{mn}_{\mathbf{k}}$ to obtain hopping matrix elements.

Performing this procedure for the two topmost Dirac bands resulting from the continuum model of Ref. [30] for twisted bilayer $WS_2$ at twist angle $3.5°$ yields the Wannier orbitals shown in Fig. 7(a). The two Wannier orbitals at sublattice $m \in \{A, B\}$ are well-localized on the scale of the moiré lattice.

The band structures from the continuum model and the Wannier tight binding model are compared in Fig. 7(b). We see that including up to three nearest-neighbor hoppings is sufficient to describe the upmost bands from the continuum model quite accurately.

For correlated electron modeling, one has to include also the interaction terms, i.e., usually Coulomb and electron-phonon interactions, to the model. We focus here on the Coulomb interactions.

Two ingredients are needed for that: the Wannier functions $\mathcal{W}_{\mathbf{R}m}(\mathbf{r})$ and an interaction kernel $V_{\text{eff}}(\mathbf{r})$ describing the effective appropriately screened Coulomb interaction. With these the (density-density part of the) Coulomb interaction matrix reads

$$W_{\mathbf{R},mn} = \iint d^2\mathbf{r}\, d^2\mathbf{r}'\; V_{\text{eff}}(\mathbf{r}-\mathbf{r}')\rho_{\mathbf{R}m}(\mathbf{r})\rho_{\mathbf{0}n}(\mathbf{r}'), \tag{11}$$

where $\rho_{\mathbf{R}m}(\mathbf{r}) = |\mathcal{W}_{\mathbf{R}m}(\mathbf{r})|^2$. In $V_{\text{eff}}(\mathbf{r})$ different screening contributions have to be accounted for: (i) the external screening by the dielectric environment and distant gate electrodes present in typical devices (Fig. 2), (ii) internal screening taking place in the $tWS_2$ bilayer, where one has to exclude those screening channels that will be later generated also in the many-body treatment of the low-energy model. While this partial internal screening has been discussed in some works like Ref. [33], a full analysis remains an open issue to date. A widely employed approximation is currently to use the Coulomb interaction screened by the TMDC bilayer in its undoped state and the dielectric environment for $V_{\text{eff}}(\mathbf{r})$.

To estimate the upper and lower bounds for the effective interaction within this approximation one can consider the following in two limiting cases for the dielectric environment: free-standing twisted bilayers, for which the external screening is minimal, and a metallic gate in direct contact with the twisted bilayers, for which the external screening is maximal [32, 33].

For practical calculations, it is helpful to start from an Ohno potential

$$V_{\text{Ohno}}(\mathbf{r}) = \frac{e^2}{\sqrt{r^2+\xi^2}} \tag{12}$$

which regularizes the bare Coulomb interaction $e^2/r$ at a short wavelength cut-off. For $tWS_2$ a natural cut-off is given by the spacial extent of the W $d$-orbitals, i.e., $\xi \approx 1$ Å. The effect of screening is easiest included in reciprocal space, so the effective interaction is $V_{\text{eff}}(\mathbf{r})$ then calculated from the inverse Fourier transformation of

$$V_{\text{eff}}(\mathbf{q}) = \frac{V_{\text{Ohno}}(\mathbf{q})}{\epsilon(\mathbf{q})} = \frac{2\pi e^2}{\epsilon(\mathbf{q})q}\mathrm{e}^{-q\xi}\,, \tag{13}$$

where $\epsilon(\mathbf{q})$ is the dielectric function that encodes the environmental screening effect. The two limiting cases, free-standing ('fs') and metal in direct contact ('m'), correspond to the effective dielectric functions [33]

$$\epsilon_{\text{fs}}(\mathbf{q}) = \kappa\frac{1-\tilde{\kappa}\mathrm{e}^{-qh}}{1+\tilde{\kappa}\,\mathrm{e}^{-qh}} \quad \text{and} \quad \epsilon_{\text{m}}(\mathbf{q}) = \kappa\coth\frac{qh}{2}\,. \tag{14}$$

Here, $\kappa \approx 10$ is the internal screening of the undoped TMDC bilayer, $h \approx 13$ Å is the bilayer height, and $\tilde{\kappa} = (\kappa-1)/(\kappa+1)$.

In Fig. 8(a) we plot the on-site and nearest-neighbor interactions, $U = W_{\mathbf{0},AA} = W_{\mathbf{0},BB}$ and $V = W_{\mathbf{0},AB}$, at different twist angles $\theta$ for the two limiting cases for $WS_2$. For for a metal gate in direct contact with the twisted $WS_2$ bilayer, the nearest-neighbor interaction $V_{\text{m}}$ is on the order of 1 meV and not included in the plot.

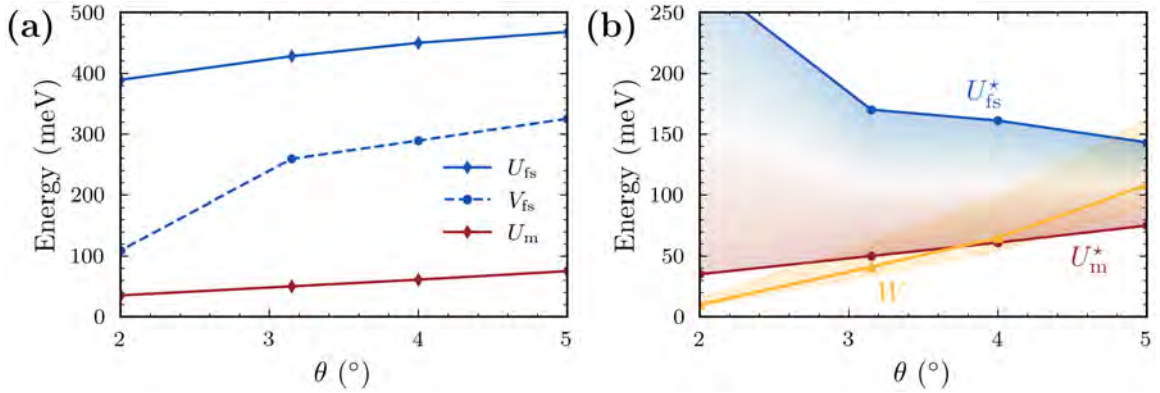


**Fig. 8:** *Estimated Coulomb interactions in different dielectric environments for twisted $WS_2$ bilayers. (a) Local and nearest-neighbor Coulomb interaction $U$ and $V$ in two dielectric environments, free-standing twisted bilayer ('fs', red line) and metallic gate in direct contact with the twisted bilayer ('m', blue line) as function of twist angle $\theta$. (b) Effective local Hubbard interactions $U^\star = U - V$ and bandwidth $W$ (orange line). The blue-red shaded region describes the possible values that $U^\star$ can take depending on the dielectric environmental setup. From Ref. [32].*

The resulting extended Hubbard models can be mapped onto a local Hubbard model with effective local interaction $U^\star$ by making the assumption $U^\star \approx U - V$ [15]. Fig. 8(b) shows $U^\star$ in comparison to the bandwidth $W$.

A realistic value for $U^\star$ in $\Gamma$-valley twisted TMDCs will fall inside the shaded regions between the limiting cases $U^\star_{\rm fs}$ and $U^\star_{\rm m}$, which depends on the experimental setup and which can be tuned by changing the dielectric environment.

Intriguing correlated electron physics with metal-insulator transitions, different kinds of spontaneous symmetry breaking including superconductivity is expected to be most prominent, where characteristic Coulomb and kinetic energy scales are on the same order of magnitude. Fig. 8 shows that twisted TMD bilayers in typical experimental setups will allow to widely tune the effective interaction strength and to reach regimes of Coulomb and kinetic energies being on the same scale.

Given the experimental state of the field we proceed with the more complex cases of twisted bilayer graphene and twisted $WSe_2$, where moiré flat bands occur due to interlayer hybridization at the corners of the Brillouin and where bands with finite Chern numbers are involved.

## 2.2 Twisted bilayer graphene

Twisted bilayer graphene (TBG) is a striking example, where the theoretical prediction [34, 35] of correlation effects predated their experimental realization [5, 6] but where the actual understanding of the system poses an outstanding challenge to theory. It illustrates thus the bidirectionality of the interplay between theory and experiment.

To rationalize the emergence of flat bands in TBG, we follow Refs. [5, 34, 35] and the corresponding cartoon shown in Fig. 9. In the absence of any interlayer coupling, the low-energy

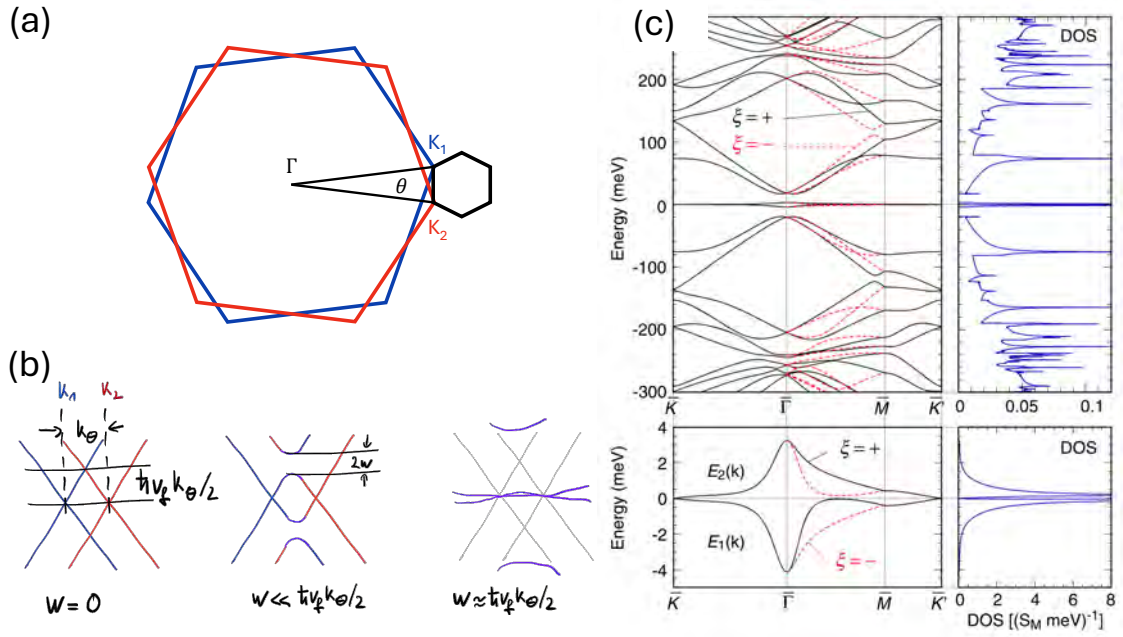


**Fig. 9:** *Moiré Brillouin zone and flat bands in magic angle TBG. (a) The moiré mini Brillouin zone is constructed from the difference between the two K (or K') wavevectors from the two layers. (b) Hybridization between Dirac cones within each valley leads to flat bands near the magic angle. Illustration of the two Dirac bands from the two layers contributing the low-energy states in each valley. The cases of vanishing interlayer hybridization (left panel), small hybridization ($2w \ll \hbar v_f k_\theta$, middle panel), and hybridization $2w \approx \hbar v_f k_\theta$ (right panel) leading to complete band flattening at the magic angle are shown. (c) Band structure and the density of states of TBG at the magic angle $\theta = 1.05°$ as obtained from the continuum model of Ref. [36]. The lower panel is the enlarged plot of the flat-band region. The black solid line and red dashed line represent the energy bands of valleys, K and K' respectively. Panel (c) from Ref. [36].*

band structure in each valley would be made up of two Dirac cones, one stemming from the lower and one stemming from the upper layer, which are rotated about the Brillouin zone center by the twist angle $\theta$. The difference between the two rotated K (or K') wavevectors gives rise to the moiré Brillouin zone, which is shown as a small hexagon in Fig. 9(a). While the Dirac cones near either of the K or K' valleys mix through interlayer hybridization, the coupling between distant Dirac cones is suppressed and "valley" remains a good quantum number.

The interlayer hybridization leads to energy gaps that open near the intersection of the Dirac cones and a renormalization of the Fermi velocity. Indeed, a series of "magic" twist angles $\theta$ emerges, where the Fermi velocity at the Dirac points vanishes.

The flattening of the energy bands near the first (and experimentally most relevant) magic angle can be understood qualitatively from the competition between the intralayer kinetic energy and the interlayer hybridization as depicted in Fig. 9(b): When the hybridization energy $2w$ becomes comparable to the intralayer kinetic energy associated with the twist induced momentum offset between the Dirac points $\hbar v_f k_\theta$, the lower of the hybridized states are pushed to zero energy leading to band flattening and the first magic angle. With $w \approx 110$ meV [35], one arrives at $\theta_M = 1.05°$ for the first magic angle.

In Fig. 9c we show a band structure and density of states (DOS) of TBG at this "magic" angle $\theta_M = 1.05^\circ$ [36]. The flat bands have a bandwidth on the order of $10\,\mathrm{meV}$ and are well separated in energy from higher-energy dispersive bands.

A usual route towards modeling the correlated states of TBG would be to proceed along the lines of the previous section, i.e., to build a Wannier tight-binding model for the flat bands and then to incorporate interactions. Typically, the relevant orbitals for the tight-binding model can be inferred from chemical intuition or from the projected density of states for the relevant bands. This approach does not work in the case of TBG, as we will see following closely Ref. [37]: One finds that the local density states for the flat bands is strongly peaked to the AA regions of the moiré [5], which form a triangular lattice. It would thus seem natural to consider a real-space model starting from effective orbitals centered at the AA sites, which corresponds to a tight-binding model defined on the triangular lattice. Treating the two valleys separately, one would arrive at a model with two orbitals localized to each of the triangular sites (i.e., AA regions of the moiré pattern).

However, such a model contradicts symmetry requirements [37] as can be seen from the band structure of TBG shown in Fig. 9(c): Per valley we have two low-energy flat bands. These are nondegenerate at $\Gamma$ but exhibit (indeed symmetry-protected) Dirac points at $\mathrm{K_M}$ and $\mathrm{K'_M}$. This pattern of degeneracies allows to infer the symmetries and Wyckoff positions of the involved orbitals. A triangular-lattice model respecting all symmetries of TBG would always lead to a situation where the two bands are either nondegenerate at all high-symmetry Brillouin zone points ($\Gamma$, $\mathrm{K_M}$, $\mathrm{K'_M}$), or all three points are Dirac points. Both patterns are inconsistent with the low-energy band structure of TBG, which rules out all "pure" triangular-lattice models [37]. Indeed, the degeneracies found in the low energy band of magic angle TBG match exactly those found in monolayer graphene. This indicates (and one can indeed show) that any tight-binding model describing the flat bands alone must correspond to orbitals sitting on a honeycomb lattice. There seems to be thus a contradiction: symmetry arguments imply Wannier centers at a honeycomb lattice, while the local density of states derived from the flat band sector peaks at triangular lattice site.

One can attempt to reconcile this problem in different ways: first, one could allow for extended Wannier functions with nontrivial shapes, where each orbital is centered at a honeycomb site (i.e., the AB/BA regions of the moiré pattern) but the weight of the orbitals is mainly localized at AA sites. Corresponding Wannier constructions have been pursued, e.g., in Ref. [36] and lead to orbitals that resemble (three-lobed) fidget spinners. Such orbitals bring along several problems: long ranged hopping, multiple sizeable non-local non-density-density general four fermion interaction terms in the Coulomb tensor, which are problematic in the DMFT context, breaking of interlayer mirror symmetries, and an incorrect representation of the topology [37].

The latter issue arises very generally when constructing tight-binding representations of moiré systems, where multiple valleys away from the $\Gamma$-point of the original single layer constituents are involved [13]. In the case of graphene it can be understood as follows.

There is a Berry phase of $\pm\pi$ for any closed loop encircling a single Dirac point. This is also the case in monolayer graphene. In monolayer graphene the Berry phase of the Dirac point at K and

K' carry opposite sign and do not obstruct any tight-binding representation of the monolayer graphene bands. In contrast, in MA-TBG the two inequivalent Dirac points stemming from the different layers but same valley as entering the single-valley model have the same winding number and thus do not add up to zero. However, the total winding number of the Dirac points arising in any (sufficiently symmetric) two-band tight-binding model would necessarily be zero. So, a tight-binding model with two localized Wannier functions per valley only, that reproduces two flat bands, preserves valley quantum numbers and TBG symmetries must not exist.
There is however a second route that turned out successful for the formulation of lattice models that respect the symmetries of MA-TBG, the topology of the low-energy flat band sector and that yield finally models that are accessible to correlated electron techniques such as DMFT. This route is based on extending the single particle Hilbert space beyond the flat band manifold. Two flavors of this route exist.

- "All Wannier models": here all degrees of freedom entering the modeling are represented through Wannier orbitals. In particular, a formulation based on two correlated and eight non-correlated orbitals per valley [38, 39] turned out successful for DMFT modeling of TBG [40]. We will discuss this approach in the context of $tWSe_2$ in section 2.3.

- "Topological heavy fermion" [41] and "projector models" [42]: in these models the correlated orbitals (i.e. two per valley) are represented in real space through proper Wannier orbitals but the additional weakly correlated electronic states contributing to the model are represented in $\mathbf{k}$-space.

We will follow here the discussion of the topological heavy fermion model for TBG along the lines of Ref. [41], noting that the resultant model will be very similar to the projector based modeling of Ref. [42]. The concept of projector based modeling is widely used in complex multiband situations arising also in bulk systems [43].
Since it is impossible to obtain a symmetry and topology respecting tight-binding model for the two flat bands alone, the idea of the topological heavy fermion model is to involve the spectral weight missing for a proper Wannierization from higher lying bands [41]. The detailed symmetry analysis performed in Ref. [41] indeed shows that this is possible by using four additional bands and working with $p_x \pm ip_y$ trial orbitals located at the triangular lattice formed by the AA sites to carry most (but not all spectral weight) of the flat bands. The overlaps of Gaussian shaped $p_x \pm ip_y$-trial orbitals and the Bloch bands of TBG are visualized in Fig. 10(b). We see that the trial orbitals are supported by the flat band states at $\mathbf{k}$ away from $\Gamma_M$ and by the lowest higher-energy bands around $\Gamma_M$. Wannierization starting from the $p_x \pm ip_y$-projectors leads to maximally localized Wannier functions with density as depicted in the inset of Fig. 10(b). The resultant Wannier functions span 96% of the flat bands and are well-localized [41].
Yet, the remaining 4% of spectral weight of the low-energy bands are very important for the phase diagram of TBG. To recover the low-energy bands including their symmetry and topology correctly, we have to augment the model with further states. We start from the continuum model Hamiltonian of TBG, $H_{BM}$, which is of referred to as the "Bistritzer MacDonald" (BM)

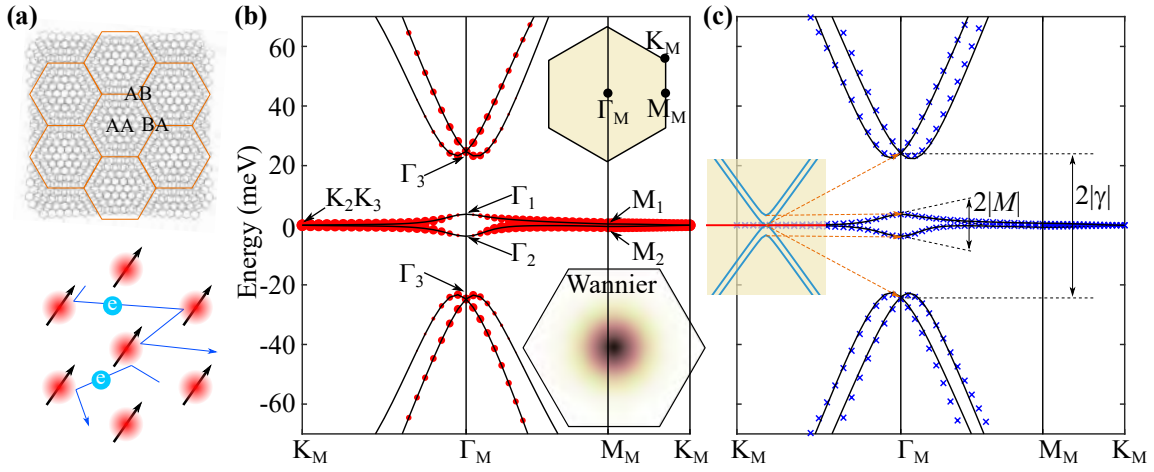


**Fig. 10:** *(a) An illustration of the moiré unit cell of TBG and the topological heavy fermion model, where the localized electrons ($f$-orbitals in the AA-stacking regions) hybridize with itinerant $c$-electrons carrying the topology. (b) The band structure of the magic angle TBG model obtained from the BM continuum model of Ref. [35]. The moiré Brillouin zone is illustrated in the upper inset. The overlaps between the Bloch states and trial $f$-orbitals are represented by the red circles. The density profile of the Wannier functions from Ref. [41] for the $f$-orbitals is shown in the lower inset. (c) Comparison of bands from the topological heavy fermion model (black lines) to the full continuum model bands (blue crosses). The inset shows the $c$- (blue) and $f$-bands (red) in the decoupled limit. Orange dashed lines indicate the evolution of energy levels as the $f$-$c$ coupling is turned on. From Ref. [41].*

model [35, 41]. We define the projector onto the space spanned by the WFs as $\mathbb{P}$, the projector into the lowest six bands (per spin and valley) as $\mathbb{I}$, and divide the low energy BM Hamiltonian $H_{BM}$ into four parts: $H^{(f)} = \mathbb{P}H_{BM}\mathbb{P}$, $H^{(c)} = \mathbb{Q}H_{BM}\mathbb{Q}$, $H^{(fc)} = \mathbb{P}H_{BM}\mathbb{Q}$, $H^{(cf)} = H^{(fc)\dagger}$, where $\mathbb{Q} = \mathbb{I} - \mathbb{P}$, $H^{(c)}$ is the remaining Hamiltonian, and $H^{(fc)} + \text{h.c.}$ is the coupling between WFs and the remaining states [41].

Since the hopping between neighboring Wannier centers is extremely weak ($\sim$0.1 meV) and it is neglected in many works: $H^{(f)} \to 0$. The analysis performed in Ref. [41] then shows that the Hamiltonian describing the six lowest energy bands then takes the form

$$H^K_{HF}(\mathbf{k}) = \begin{pmatrix} H^{(c)} & H^{(cf)} \\ H^{(fc)} & H^{(f)} \end{pmatrix} = \begin{pmatrix} 0 & v\mathbf{k}\cdot(\sigma_0, i\sigma_3) & \gamma\sigma_0 + v'\mathbf{k}\cdot\boldsymbol{\sigma} \\ v\mathbf{k}\cdot(\sigma_0, -i\sigma_3) & M\sigma_1 & 0 \\ \gamma\sigma_0 + v'\mathbf{k}\cdot\boldsymbol{\sigma} & 0 & 0 \end{pmatrix}. \quad (15)$$

Choosing the parameters $v_\star$=$-$4.303 eV·Å, $M$=3.697 meV, $\gamma$=$-$24.75 meV, $v'_\star$=1.622 eV·Å, the low-energy band structure of TBG turns out to be well-matched by the Hamiltonian of Eq. (15) (see Fig. 9(c)).

In the model reproduced here, the Wannier functions are strongly localized and hybridize with delocalized topological highly dispersive electronic states. These states are usually referred to as $f$- and $c$-electrons, respectively. This situation resembles heavy fermion materials and the model of Eq. (15) is named "topological heavy fermion (THF) model" of TBG [41].

### 2.2.1 Coulomb interaction in the topological heavy fermion model

From the construction of the THF model the wave functions of the $f$ states and the $c$ states are known and one can obtain all Coulomb matrix elements as required for modeling of electronic correlation effects.

The $f$ electrons have a real-space and a $k$-space representation, while the $c$-electron have a $k$-space representation only. This needs to be taken into account when calculating the Coulomb integrals.

We note here two points that are of particular importance, when deriving Coulomb terms for moiré systems. First, the Coulomb interaction of 2D materials can be strongly impacted and controlled by the dielectric environment of the material—a concept sometimes called Coulomb engineering. Experiments on TBG typically work with single or doubled gate structures, where the actual TBG layer is separated by hBN spacer layers from metallic some gate electrodes. An appropriately screened Coulomb interaction to enter a low energy model of TBG should account for both, the internal and the external screening [33]. The Coulomb interaction derived in Ref. [41] accounts for screening by the hBN and a typical double gate structure (cf. Fig.2).

For this configuration one arrives at the following Coulomb interaction terms in the THF model

$$\hat{H}_I = \hat{H}_{U_1} + \hat{H}_J + \hat{H}_{U_2} + \hat{H}_V + \hat{H}_W \tag{16}$$

$\hat{H}_{U_1} = \frac{U_1}{2} \sum_{\mathbf{R}} :\rho^f_{\mathbf{R}}: :\rho^f_{\mathbf{R}}:$ are the on-site interactions of $f$-electrons with $\rho^f_{\mathbf{R}}$ being the $f$-electron density operator at site $\mathbf{R}$ and the colon symbols represent the normal ordered operator with respect to the normal state. $\hat{H}_J$ is a ferromagnetic exchange coupling between the $f$- and the $c$-electrons. Using a typical setup for MATBG, Ref. [41] finds $U_1 = 57.95\,\text{meV}$ and $J = 16.38\,\text{meV}$ setting the scale of $\hat{H}_J$. The other three terms in $\hat{H}_I$ are: $H_{U_2}$, the repulsion ($\sim 2.3\,\text{meV}$) between nearest neighbor $f$-electrons, $H_V$, the repulsion ($\sim 48\,\text{meV}$) between $c$-electrons, and $H_W$, the repulsion ($\sim 47\,\text{meV}$) between $c$- and $f$-electrons.

A usually adopted approximation motivated by the respective band widths of the $c$- and $f$-electrons is to treat only the local $f$-$f$ interactions ($\hat{H}_{U_1}$) dynamically but all other interactions at a static Hartree(-Fock) level. Then, $H_{U_2} + H_V + H_W$ will effectively only shift the band energies of the entire $c$- and $f$-block relative to each other.

From the numbers above it becomes clear that the Hartree terms relating to $H_V$ and $H_W$ are by no means small. Indeed, there are substantial shifts between the $f$- and the $c$-block upon changing the filling as can be seen from the Hartree Fock band structures taken from Ref. [41], which we reproduce here in Fig. 11. Thus, when attempting to model electronic correlation phenomena, it is very important to consider also these additional interaction terms.

### 2.2.2 DMFT implementation for twisted bilayer graphene

We follow now [44] to explain, how one can proceed from the THF model towards practical DMFT simulations of TBG. First, we split the total Hamiltonian into a static and a dynamic

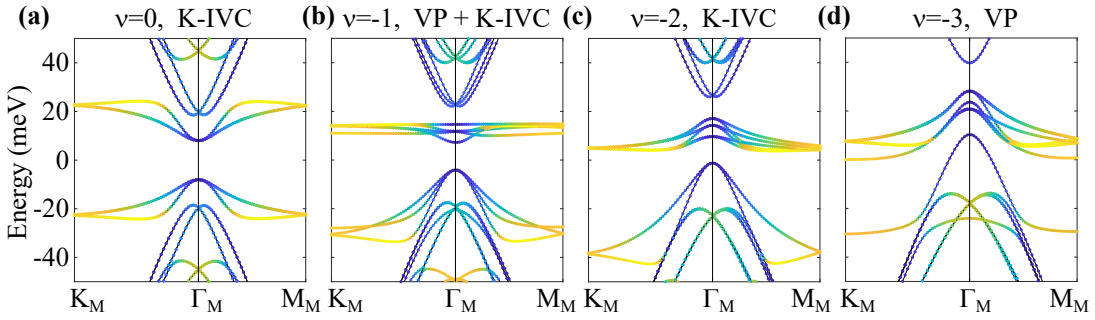


**Fig. 11:** *Band structure obtained from Hartree Fock solutions of the topological heavy fermion model at fillings $\nu = 0, -1, -2, -3$. The color of the bands represents their orbital composition with $f$-electron states printed in yellow and $c$-electrons states in blue. From Ref. [41].*

part,

$$\hat{H}_{\text{stat}} = \hat{H}_c + \hat{H}_{fc} + \hat{H}_W^{MF} + \hat{H}_V^{MF} + \hat{H}_J^{MF} - 3.5U \sum_{\alpha\eta\sigma} f^\dagger_{\alpha\eta\sigma} f_{\alpha\eta\sigma}, \tag{17}$$

$$\hat{H}_{\text{dyn}} = \frac{U}{2} \sum_{(\alpha\eta\sigma)\neq(\alpha'\eta'\sigma')} f^\dagger_{\alpha\eta\sigma} f_{\alpha\eta\sigma} f^\dagger_{\alpha'\eta'\sigma'} f_{\alpha'\eta'\sigma'}. \tag{18}$$

The superscript $MF$ represents a static mean-field decoupled interaction term (Hartree+Fock for $\hat{H}_W^{MF}$ and $\hat{H}_J^{MF}$ and Hartree for $\hat{H}_V^{MF}$).
$\hat{H}_{\text{stat}}$ plays the role of the lattice Hamiltonian in the DMFT calculation. It must be self-consistently determined, as the mean-field decoupled interaction terms depend on the system's density matrix $\rho$. $\hat{H}_{\text{dyn}}$ acts on the $f$-subspace only and induces a frequency-dependent self-energy in the $f$-subspace. The self-energy for the $f$-sector is obtained from solving the impurity problem arising in DMFT with some appropriate solver. For the TBG problem at hand continuous-time quantum Monte Carlo (CT-QMC) hybridization expansion solvers turn out to be practicable [44]. Importantly, one has to converge two nested self-consistency loops: the DMFT self-consistency for the self-energy $\Sigma$ of the $f$-subspace and the Hartree-Fock self-consistency setting $\hat{H}_W^{MF}$, $\hat{H}_J^{MF}$ and $\hat{H}_V^{MF}$. This computational scheme thus resembles charge-self-consistent DMFT calculations known from the DFT+DMFT context.

## 2.3 Twisted bilayer $WSe_2$

Twisted bilayer $WSe_2$ has been demonstrated experimentally to host intriguing correlated electron physics including metal insulator transitions in close vicinity to superconductivity as explained in section 1.2.
Here, the moiré bands emerge at the valence band edge in the K and K' valley, i.e., at non-time reversal invariant points of the Brillouin zone, with the valley index being a good quantum number in the band structure part of the moiré Hamiltonian. This situation is akin to TBG. Again, the moiré bands for each valley can carry finite Chern numbers, while Chern numbers from opposite valleys would cancel. Thus, also here topology can obstruct Wannierization and impact the emergent electron correlations by enforcing admixture of different orbitals to, e.g., the highest moiré band.

We lay out here, the "all Wannier model" approach for model building mentioned already for TBG. We follow closely Refs. [45, 46] giving an application to twisted $WSe_2$. The procedure is to (i) start from a large-scale model (here a continuum model), (ii) build proper Wannier functions, and (iii) obtain appropriate interaction terms to arrive at an extended multiorbital Hubbard model.

The non-interacting electronic structure of hole-doped t$WSe_2$ is accurately described by a continuum model in which the spin-valley locked holes of both monolayers are treated within an effective mass approximation, and are coupled by moiré potentials and interlayer tunneling. For the spin-up sector of the $K$ the continuum Hamiltonian is a matrix in layer space reading

$$H(\boldsymbol{k}) = \begin{pmatrix} (\boldsymbol{k}-\kappa)^2/2m^* + \Delta_+(\boldsymbol{r}) & T_M(\boldsymbol{r}) \\ T_M^\dagger(\boldsymbol{r}) & (\boldsymbol{k}-\kappa')^2/2m^* + \Delta_-(\boldsymbol{r}) \end{pmatrix} + \begin{pmatrix} E_z & 0 \\ 0 & -E_z \end{pmatrix}. \tag{19}$$

Here, $m^*$ is the hole effective mass from the $WSe_2$ monolayer and $E_z$ accounts for external out-of-plane electric fields in the form of a layer-dependent potential. The $\kappa$ and $\kappa'$ points denote the position of the $K$-point coming from the top and bottom layer, respectively, which are displaced due to the twist. The intra- and inter-layer moiré couplings read $\Delta_\pm(\boldsymbol{r}) = V \sum_{\boldsymbol{g}\in\hexagon} \cos(\boldsymbol{g}\cdot\boldsymbol{r} \pm \psi)$ and $T_M(\boldsymbol{r}) = w\left(1 + e^{i\boldsymbol{g}_1\cdot\boldsymbol{r}} + e^{i\boldsymbol{g}_2\cdot\boldsymbol{r}}\right)$ [47]. The parameters $V$, $\psi$, and $w$ characterizing the moiré couplings can be obtained by fitting Eq. (19) to large-scale *ab-initio* calculations [48] and are given in Refs. [45–47].[1]

For the DMFT modeling we seek a Wannier representation of the topmost valence bands. A symmetry analysis [49, 50] suggests a model with three Wannier orbitals per valley and unit cell, where one of these is centered at triangular lattice site $T$, having weight on both layers, as well as the others at two honeycomb lattice sites $H_{1,2}$ with dominant weight on either one of the layers as depicted in Fig. 12.

In the twist angle range $3.5^\circ < \theta < 5^\circ$, however, the Chern number sequence of the first three valence bands of t$WSe_2$ in valley $\nu = \pm 1$ is $(\nu, \nu, \nu)$ for the parameters of Ref. [48], prohibiting an exponential localization of these three bands alone onto the (in total three) $T$ and $H_{1,2}$ sites. To resolve this issue, one can adapt the "single shot" Wannierization procedure outlined in section 2.1 in the following way [31, 39, 46, 51]: Instead of having as many Bloch states as Wannier states, we consider Bloch states from the entire valence band manifold for the projection. For a proper subspace selection, the Bloch states will be weighted according to their energy.

The construction works as follows: We start we $N$ trial orbitals $|g^m\rangle$ and replace the projection of Eq. (6) by an energy-weighted "projection"[2]

$$|\phi_{\boldsymbol{k}}^m\rangle = \sum_{\alpha=1}^{M} |\Phi_{\boldsymbol{k}}^\alpha\rangle\, w_{\alpha\boldsymbol{k}}\, \langle \Phi_{\boldsymbol{k}}^\alpha | g^m\rangle\,. \tag{20}$$

The sum involves more Bloch states $|\Phi_{\boldsymbol{k}}^\alpha\rangle$ (i.e. eigenstates of the Hamiltonian $H$ from Eq. (19)) than trial functions $M > N$ and $w_{\alpha\boldsymbol{k}} \in [0, 1]$ is a weighting factor for the Bloch states to

[1] The '$\hexagon$' denotes the set of the first shell of moiré reciprocal lattice vectors, and $\boldsymbol{g}_{1,2}$ are two reciprocal lattice vectors in the first shell rotated by $60^\circ$ with respect to each other.

[2] We note that Eq. (20) is not a projection in the strict mathematical sense.

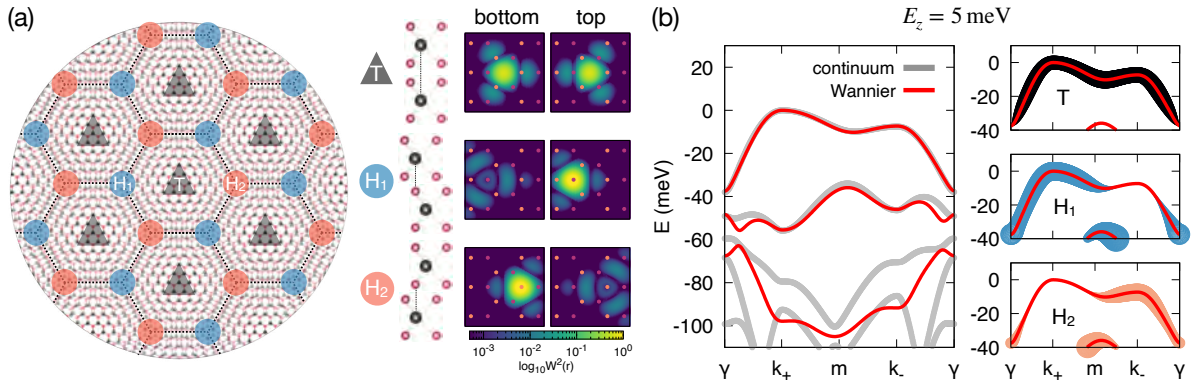


**Fig. 12:** *(a) Sketch of the local stacking regions, MM (T), MX ($H_1$), and XM ($H_2$), in the moiré lattice of $tWSe_2$ and the corresponding Wannier functions on the top layer and the bottom layer at $E_z = 0$. (b) Three-orbital Wannier bands for one valley/spin ($\sigma = \uparrow$) overlaid with continuum model bands at $E_z = 5$ meV along with the corresponding spectral weight of Wannier orbitals in the topmost band. The opposite valley/spin ($\sigma = \downarrow$) states are obtained via time-reversal conjugation of the $\uparrow$ states. Adapted from Ref. [45].*

facilitate band disentanglement. For the example of $tWSe_2$, Ref. [46] applied an exponential weighting scheme

$$w_\alpha(\boldsymbol{k}) = e^{-|\epsilon_\alpha(\boldsymbol{k})|/\eta} \tag{21}$$

with $\eta = 80\,\mathrm{meV}$.

The choice of a proper trial functions and of a proper weighting scheme is indeed central to the model building. Once, both is achieved, one can continue from Eq. (20) with the standard Wannierization scheme [31] outlined in section 2.1. Hereby, when obtaining the overlap matrix according to Eq. (7), one can either calculate $S^{mn}_{\mathbf{k}}$ with an explicit representation of the $|\phi^m_{\boldsymbol{k}}\rangle$ from Eq. (20) or using adapted "projector" matrices $P^{\alpha m}_{\mathbf{k}} = w_\alpha(\boldsymbol{k})\,\langle \Phi^\alpha_{\mathbf{k}} | g^m \rangle$.

For the case of twisted bilayer $WSe_2$ at twist angle $3.15°$, Fig. 12 shows the Wannier functions resulting from this adapted procedure and a comparison between the continuum model and the three orbital Wannier model. We see that the topmost moiré band is well reproduced by the Wannier model and that indeed all three orbitals contribute to this topmost band. The third continuum band does not match the third Wannier model band. Indeed, admixtures of states from the fourth and higher bands are essential for a three-orbital description, which has to yield an overall vanishing *total* Chern number in contrast to the three lowest lying bands of the continuum model. The lattice model reproduced here, has been used to analyze electron correlations and spontaneous symmetry breaking in twisted $WSe_2$ bilayers in Refs. [45, 46, 52].

# 3 DMFT studies of correlations in moiré systems

There are two major differences in DMFT of modeling moiré quantum materials as compared to bulk systems: (i) the more complex model building (cf. section 2) and (ii) the experimental tunabilities particularly via gate voltages allowing to change the number of electrons by as much as one electron (or even more) per (moiré) unit cell. Due to the latter it is often critical to account

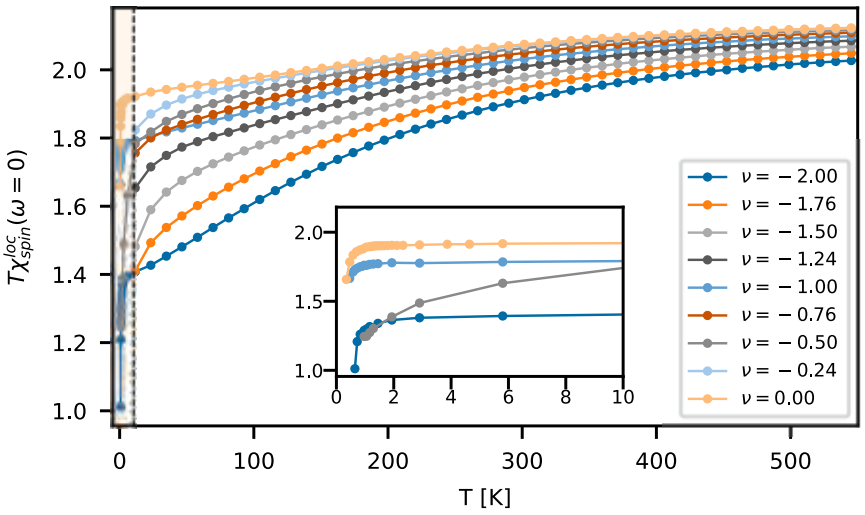


**Fig. 13:** *Local static spin susceptibility in the symmetric phase of TBG as a function of temperature. The shaded region of the main panel, delimited by the black dashed line is enlarged in the inset and illustrates the Curie-Weiss susceptibility plateau, associated with the presence of local moments at integer fillings. From Ref. [44].*

of charge self-consistency in the modeling. In the following we exemplify some insights that can be gained from the DMFT and related many-electron modeling of TBG and $tWSe_2$. This section is not meant to be exhaustive review of the field but more an introduction showcasing some phenomena that can be understood from many-body modeling of moiré systems.

## 3.1 Twisted bilayer graphene

DMFT studies using all Wannier models [40, 53], projector techniques [42] and the topological heavy fermion model [44,54–56] of TBG gave explanations and deeper understanding of several correlation effects seen in TBG experiments.

To understand the physics taking place across the temperature scale from $\mathcal{O}(100\,\mathrm{K})$ down to $\mathcal{O}(5\,\mathrm{K})$ we consider the spin-susceptibility and follow closely the discussion from Ref. [44]: In a non-interacting system, we would expect a Pauli type behavior, $\chi^{\mathrm{loc}}_{\mathrm{spin}}(T) \sim const.$, for the temperature dependence of the local spin susceptibility. In an interacting system, local (iso)spin moments are formed when charge fluctuations are suppressed due to Coulomb energy penalties. This reflects in the Curie-like behavior of the local spin susceptibility $\chi^{\mathrm{loc}}_{\mathrm{spin}}(T) \sim 1/T$. From deviations of $\chi^{\mathrm{loc}}_{\mathrm{spin}}(T)$ from the Curie law, one can identify two temperature scales: $T_{\mathrm{K}}$, below which Kondo screening takes place, and $T_{\mathrm{Moments}}$, above which thermally activated charge fluctuations set in. In the simplest case of a one-orbital model, charge fluctuations lead to the doubly-occupied and empty sectors contributing significantly to the partition function. This range of very high temperatures, known as *free orbital regime*, is associated with a decrease in the $1/T$-coefficient of $\chi^{\mathrm{loc}}_{\mathrm{spin}}(T)$ and an increase in entropy from $\sim \log 2$ to $\sim \log 4$, reflecting the higher number of contributing local eigenstates.

TBG features deviations from this picture in the low and in the high temperature limit. This is a consequence of the multi-orbital structure of the narrow bands manifold combined with

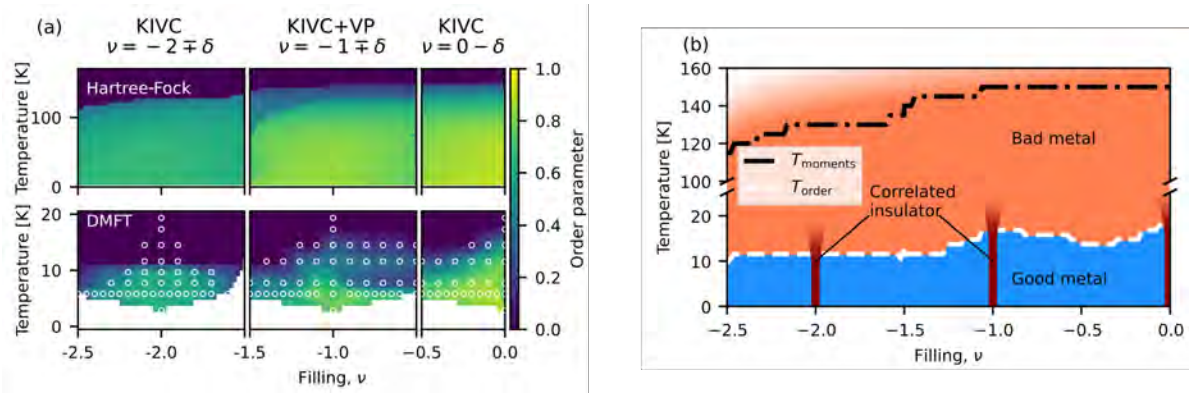


**Fig. 14:** *(a) The magnitude of the symmetry-breaking order parameter at various fillings and temperatures. In the bottom panel, white circles represent numerical data points from DMFT simulations with linear interpolation in between. The top panel shows the same quantity from a Hartree-Fock simulation (note the different vertical scale). In the dark blue regions, the self-consistency loop flows to the symmetric state, indicating that the symmetry-broken solution does not exist. (b) A schematic filling-temperature phase diagram: thermally activated charge fluctuations are frozen below the Hartree-Fock ordering temperature ($T_{moments}$), allowing local moments to progressively form in the orange region. These local moments order below the DMFT ordering temperature ($T_{order}$) in the blue region. The DMFT ordering temperature marks the boundary between a bad metal and an order-facilitated good metal at fractional fillings. The correlated insulators at integer fillings emerging below $T_{order}$ (dark red) fade into the bad metal above $T_{order}$. From Ref. [44].*

the absence of an interaction term enforcing the Hund's rules. We show $T \cdot \chi^{\mathrm{loc}}_{\mathrm{spin}}(\omega{=}0)$, which quantifies the fluctuating local moment, obtained from DMFT in the symmetric phase in Fig. 13. As can be seen from the inset, TBG at integer filling shows Curie-like behavior (i.e. the curve is horizontal) all the way down to 1–2 K. The susceptibility deviates from clear Curie behavior for all fillings when considering the temperature scale $\mathcal{O}(100\,\mathrm{K})$. The deviation from the Curie law at low-temperatures signals Kondo screening, which sets in at $\sim 2\,\mathrm{K}$ at integer filling and at higher temperatures at fractional fillings.

DMFT allows to assess the interplay of spontaneous symmetry breaking and dynamical correlations by analyzing in which part of the temperature-doping phase space a symmetry broken state is a stable solution of the self-consistency condition. A comparison, of temperature and doping dependent isospin order obtained from DMFT and Hartree Fock is given in Fig. 14. In DMFT, the system flows to the symmetric phase under the self-consistency loop for sufficiently high temperature, while order set in below threshold temperatures of $\mathcal{O}(10\,\mathrm{K})$. The ordering temperatures predicted by Hartree-Fock are an order of magnitude higher ($\sim$ 100–150 K; see upper panel of Fig. 14(a)).

The DMFT simulations show that long-range order is suppressed by local dynamic fluctuations down to about 10 K. Order is most prominent at integer fillings resulting in dome-shaped ordered regions peaked around integer fillings as seen in the lower panel of Fig. 14.

The Hartree-Fock ordering temperature encodes the onset of thermally activated charge fluctuations. Above this temperature thermal smearing results in the Hartree-Fock equations converging to the symmetric unpolarized solution. Since Hartree-Fock neglects dynamic fluctuations,

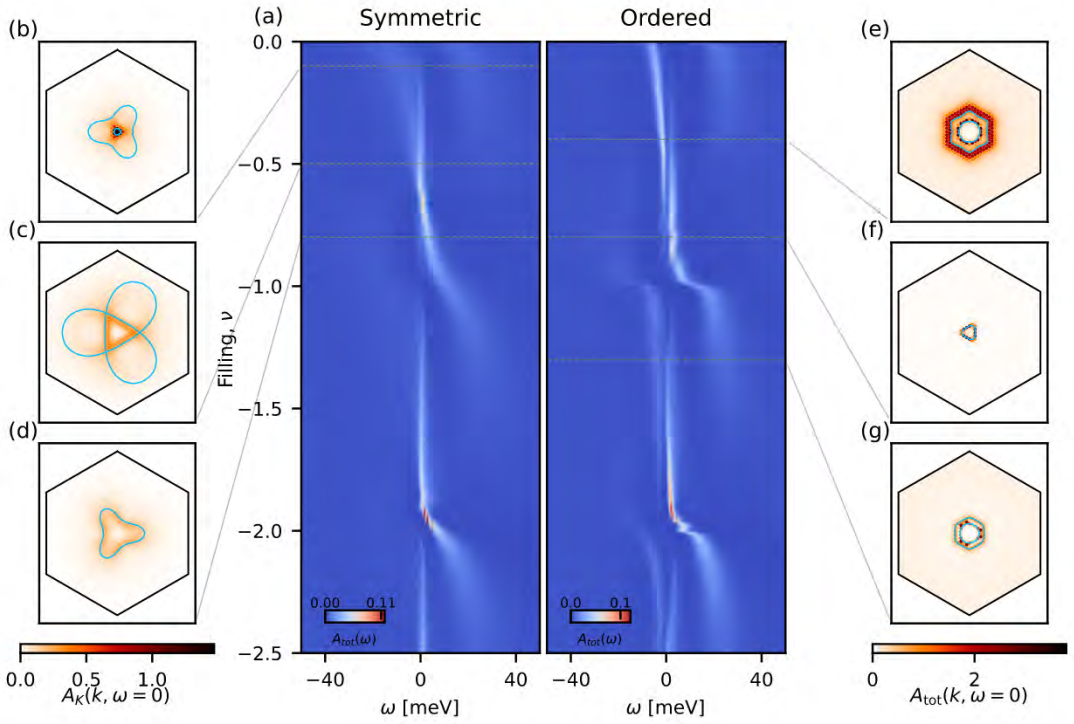


**Fig. 15:** *(a) The momentum-integrated spectral function $A_{tot}(\omega)$ 5.8 $K$ in the symmetric phase (left) and in the ordered phase (right) as a function of hole doping. The electron-doped side (with respect to CNP) is related to the hole-doped side by a particle-hole transformation. (b)-(d) The $K$-valley–projected zero-energy spectral function in the first moiré Brillouin zone in the symmetric phase at select fillings. (e)-(g) The full zero-energy spectral function in the first moiré Brillouin zone in the ordered state at select fillings. The light blue lines mark the zeros of the effective Hamiltonian as identified by a quasiparticle analysis. From Ref. [44]*

moments order immediately upon formation. Therefore, the temperature range between the Hartree-Fock and DMFT ordering temperatures is the regime of fluctuating local moments at integer fillings. Correspondingly, in this temperature range, the local spin susceptibility follows the Curie-Weiss law as seen in Fig. 13. Near half-integer filling an intermediate valence regime with quantum charge fluctuations between two neighboring sectors is realized below the Hartree-Fock ordering temperature preventing the identification of well-defined local moments. Taken together, this analysis shows the formation of local spin and valley isospin moments around 100 K for integer fillings, intermediate valence behavior in between and the ordering of the local isospin moments around 10 K [44].

DMFT naturally yields electronic spectral functions. In Fig. 15(a), we show the momentum-integrated spectral function of TBG as a function of filling in the symmetric and symmetry-broken phases. In both cases, there is a depletion of spectral weight at the Fermi level for integer $\nu$. In the symmetry broken states there are even full gaps at integer $\nu$, which explain the correlated insulating states in experiments. Upon sweeping the filling through a larger range, there is a cascadic reshuffling of the low-energy spectral weight upon changing $\nu$ by an integer value. These are the *cascade transitions* that have been seen experimentally with scanning tunneling spectroscopy (STS) [57]. These cascades have been consistently seen in DMFT studies using pure Wannier [40] and the topological heavy fermion model [44].

The symmetry-broken state behaves the same way except that there is fine low-energy structure, owing to isospin order. In particular, the zero-energy peak at fractional fillings, made up primarily of $f$-spectral weight, is split by a feedback effect from the exchange interaction $\hat{H}_J$.
Further phenomena, that can be understood from DMFT modeling of TBG include compressibilities, details of the metal insulator transitions taking place in TBG, and doping as well as temperature dependencies of quasi particle scattering rates [44]. The latter becomes clear from the k-resolved plots of the zero energy spectral weight in Fig. 15: For the symmetric state we see largely incoherent "blurry" spectral weight in space, while there much sharper Fermi contours emerge upon ordering in the system. I.e., there is "coherence from order" upon lowering the temperature in TBG, which also explains the Pomeranchuk physics observed in experiments of Refs. [58, 59].
Overall, DMFT draws the phase diagram as shown in Fig. 14(b): Below the ordering temperature of $\sim$10 K, there are insulators at integer fillings and a good metal featuring well-defined coherent quasiparticles at fractional fillings. Above the ordering temperature, the spectral weight at the Fermi level is generically incoherent, indicating a bad metal [44].

## 3.2 Twisted bilayer $WSe_2$

For $tWSe_2$, several aspects of the experiments reported in Refs. [8, 10, 11] can be understood, based on the three orbital Wannier model discussed in section 2.3. Ref. [46] performed a functional renormalization group study of this model and finds an interplay of so-called intervalley-coherent antiferromagnetic order with superconductivity. The phase boundaries as function of displacement field and doping are in good agreement with experimental observations particularly for twist angle $\sim 5^\circ$. Taken together with the Hartree Fock study of Ref. [52], it is very plausible that in the regime of twist angles $\sim 5^\circ$ a Slater-type mechanism leads to the intervalley-coherent antiferromagnetic order for certain parts of the phase diagram, while corresponding dynamical quantum fluctuations act as pairing glue for the superconducting state that emerges upon suppression of the intervalley-coherent antiferromagnetic order. Yet, temperature dependencies remain to be explored and understood here.
For twist angles of $3.5^\circ$ stronger electron correlations are expected. Ref. [45] reports a DMFT study of this system and reveals the importance of orbital polarization effects, which are strongly enhanced by Coulomb interactions: a correlated metal competes with three distinct site-polarized correlated insulators that are controllable by displacement field and dielectric constant. The insulators turn out to be charge transfer insulators, which are characterized by a strong differentiation between orbitals with regard to the correlation strength which naturally explain key experimental observations including the displacement field driven metal-to-insulator transitions, transport asymmetry, and a coherence-incoherence crossover and importantly temperature dependencies of transport.
Thus, the situation is currently such that different approaches (Hartree Fock, fRG, DMFT) explain different aspects of the correlated electron physics emerging in $tWSe_2$, while a full unified theory explaining all experiments consistently remains to be developed.

# 4 Summary

Moiré systems constitute an emerging platform for electronic quantum matter, where electron correlations arise on the length scale of the moiré superlattice. Particularly interesting is the connection between correlation phenomena and topology observed across various moiré systems, including twisted graphene structures and transition metal dichalcogenide multilayers. Both platforms exhibit rich multiorbital physics, manifested in flat electronic bands characterized by nontrivial Berry curvature and quantum geometry.
The fact that electronic correlations emerge at mesoscopic length scales enables extensive tunability via gate voltages, twist angles, and the dielectric environment. This tunability is highly advantageous for both understanding and controlling correlated electronic phases, as well as for the development of quantitative theories of correlated electron systems. These prospects have spurred extensive efforts toward many-body modeling of moiré quantum matter, including DMFT.
From a practitioner's perspective, DMFT modeling of moiré systems can be conducted in close analogy to that of conventional solids, provided that special attention is paid to the following aspects:

1. **Model Construction:** It is essential to derive faithful, well-localized Wannier functions that accurately describe the correlated orbitals. The effective low-energy model must respect the system's underlying topology and symmetries.

2. **Coulomb Interactions:** Moiré systems are typically embedded in complex dielectric environments, which have to be accounted for in the derivation of appropriate Coulomb interaction tensors.

3. **Charge Self-Consistency and Long-Range Interactions:** The filling of moiré minibands can be widely tuned—by as much as one or more electrons per moiré unit cell—using gate voltages. This variability leads to substantial effects arising from the interplay between local and non-local Coulomb terms in multi-orbital and/or multi-site systems, which must be accurately captured in charge self-consistent DMFT calculations.

The field is now approaching a quantitative understanding of the phase diagrams, excitation spectra, and transport properties of moiré systems. In this context, DMFT has proven capable of delivering semi-quantitative insights into thermodynamic observables and spectral properties, as illustrated in section 3. Key open challenges include achieving a precise and quantitative understanding of superconductivity, quantum criticality, and strange metal behavior in moiré systems, as well as incorporating non-local correlation effects.

# References


[1] A.K. Geim and I.V. Grigorieva, Nature **499**, 419 (2013)

[2] K.S. Novoselov, A. Mishchenko, A. Carvalho, and A.H.C. Neto, Science **353**, aac9439 (2016)

[3] A.H. Castro Neto, F. Guinea, N.M.R. Peres, K.S. Novoselov, and A.K. Geim, Rev. Mod. Phys. **81**, 109 (2009)

[4] M.I. Katsnelson: *The Physics of Graphene* (Cambridge University Press, 2020), 2 ed.

[5] Y. Cao, V. Fatemi, A. Demir, S. Fang, S.L. Tomarken, J.Y. Luo, J.D. Sanchez-Yamagishi, K. Watanabe, T. Taniguchi, E. Kaxiras, R.C. Ashoori, and P. Jarillo-Herrero, Nature **556**, 80 (2018)

[6] Y. Cao, V. Fatemi, S. Fang, K. Watanabe, T. Taniguchi, E. Kaxiras, and P. Jarillo-Herrero, Nature **556**, 43 (2018)

[7] L. Balents, C.R. Dean, D.K. Efetov, and A.F. Young, Nat. Phys. **16**, 725 (2020)

[8] L. Wang, E.-M. Shih, A. Ghiotto, L. Xian, D.A. Rhodes, C. Tan, M. Claassen, D.M. Kennes, Y. Bai, B. Kim, K. Watanabe, T. Taniguchi, X. Zhu, J. Hone, A. Rubio, A.N. Pasupathy, and C.R. Dean, Nat. Mater. **19**, 861 (2020)

[9] K.F. Mak and J. Shan, Nat. Nanotechnol. **17**, 686 (2022)

[10] Y. Xia, Z. Han, K. Watanabe, T. Taniguchi, J. Shan, and K.F. Mak, Nature **637**, 833 (2025)

[11] Y. Guo, J. Pack, J. Swann, L. Holtzman, M. Cothrine, K. Watanabe, T. Taniguchi, D.G. Mandrus, K. Barmak, J. Hone, A.J. Millis, A. Pasupathy, and C.R. Dean, Nature **637**, 839 (2025)

[12] K.P. Nuckolls and A. Yazdani, Nat. Rev. Mater. **9**, 460 (2024)

[13] P.C. Adak, S. Sinha, A. Agarwal, and M.M. Deshmukh, Nat. Rev. Mater. **9**, 481 (2024)

[14] T.O. Wehling, E. Şaşıoğlu, C. Friedrich, A.I. Lichtenstein, M.I. Katsnelson, and S. Blügel, Phys. Rev. Lett. **106**, 236805 (2011)

[15] M. Schüler, M. Rösner, T.O. Wehling, A.I. Lichtenstein, and M.I. Katsnelson, Phys. Rev. Lett. **111**, 036601 (2013)

[16] Y. Cao, D. Chowdhury, D. Rodan-Legrain, O. Rubies-Bigorda, K. Watanabe, T. Taniguchi, T. Senthil, and P. Jarillo-Herrero, Phys. Rev. Lett. **124**, 076801 (2020)

[17] X. Lu, P. Stepanov, W. Yang, M. Xie, M.A. Aamir, I. Das, C. Urgell, K. Watanabe, T. Taniguchi, G. Zhang, A. Bachtold, A.H. MacDonald, and D.K. Efetov, Nature **574**, 653 (2019)

[18] M. Yankowitz, S. Chen, H. Polshyn, Y. Zhang, K. Watanabe, T. Taniguchi, D. Graf, A.F. Young, and C.R. Dean, Science **363**, 1059 (2019)

[19] H. Polshyn, M. Yankowitz, S. Chen, Y. Zhang, K. Watanabe, T. Taniguchi, C.R. Dean, and A.F. Young, Nat. Phys. **15**, 1011 (2019)

[20] S. Wu, Z. Zhang, K. Watanabe, T. Taniguchi, and E.Y. Andrei, Nat. Mater. **20**, 488 (2021)

[21] M. Serlin, C.L. Tschirhart, H. Polshyn, Y. Zhang, J. Zhu, K. Watanabe, T. Taniguchi, L. Balents, and A.F. Young, Science **367**, 900 (2020)

[22] K.P. Nuckolls, R.L. Lee, M. Oh, D. Wong, T. Soejima, J.P. Hong, D. Călugăru, J. Herzog-Arbeitman, B.A. Bernevig, K. Watanabe, T. Taniguchi, N. Regnault, M.P. Zaletel, and A. Yazdani, Nature **620**, 525 (2023)

[23] Y. Zhang, R. Polski, C. Lewandowski, A. Thomson, Y. Peng, Y. Choi, H. Kim, K. Watanabe, T. Taniguchi, J. Alicea, F. von Oppen, G. Refael, and S. Nadj-Perge, Science **377**, 1538 (2022)

[24] Y. Xu, S. Liu, D.A. Rhodes, K. Watanabe, T. Taniguchi, J. Hone, V. Elser, K.F. Mak, and J. Shan, Nature **587**, 214 (2020)

[25] X. Huang, T. Wang, S. Miao, C. Wang, Z. Li, Z. Lian, T. Taniguchi, K. Watanabe, S. Okamoto, D. Xiao *et al.*, Nat. Phys. **17**, 715 (2021)

[26] S. Ryee and T.O. Wehling, Nano Lett. **23**, 573 (2023)

[27] A. Ghiotto, E.-M. Shih, G.S. Pereira, D.A. Rhodes, B. Kim, J. Zang, A.J. Millis, K. Watanabe, T. Taniguchi, J.C. Hone *et al.*, Nature **597**, 345 (2021)

[28] T. Li, S. Jiang, L. Li, Y. Zhang, K. Kang, J. Zhu, K. Watanabe, T. Taniguchi, D. Chowdhury, L. Fu *et al.*, Nature **597**, 350 (2021)

[29] W. Zhao, B. Shen, Z. Tao, Z. Han, K. Kang, K. Watanabe, T. Taniguchi, K.F. Mak, and J. Shan, Nature **616**, 61 (2023)

[30] M. Angeli and A.H. MacDonald, Proc. Natl. Acad. Sci. **118** (2021)

[31] N. Marzari, A.A. Mostofi, J.R. Yates, I. Souza, and D. Vanderbilt, Rev. Mod. Phys. **84**, 1419 (2012)

[32] N. Witt, J.M. Pizarro, J. Berges, T. Nomoto, R. Arita, and T.O. Wehling, Phys. Rev. B **105**, L241109 (2022)

[33] J.M. Pizarro, M. Rösner, R. Thomale, R. Valentí, and T.O. Wehling, Phys. Rev. B **100**, 161102 (2019)

[34] J.M.B. Lopes dos Santos, N.M.R. Peres, and A.H. Castro Neto, Phys. Rev. Lett. **99**, 256802 (2007)

[35] R. Bistritzer and A.H. MacDonald, Proc Natl Acad Sci USA **108**, 12233 (2011)

[36] M. Koshino, N.F. Yuan, T. Koretsune, M. Ochi, K. Kuroki, and L. Fu, Phys. Rev. X **8**, 031087 (2018)

[37] H.C. Po, L. Zou, A. Vishwanath, and T. Senthil, Phys. Rev. X **8**, 031089 (2018)

[38] H.C. Po, L. Zou, T. Senthil, and A. Vishwanath, Phys. Rev. B **99**, 195455 (2019)

[39] S. Carr, S. Fang, H.C. Po, A. Vishwanath, and E. Kaxiras, Phys. Rev. Res. **1**, 033072 (2019)

[40] A. Datta, M.J. Calderón, A. Camjayi, and E. Bascones, Nat. Commun. **14**, 5036 (2023)

[41] Z.-D. Song and B.A. Bernevig, Phys. Rev. Lett. **129**, 047601 (2022)

[42] M. Haule, E.Y. Andrei, and K. Haule, arXiv:1901.09852

[43] B. Amadon, F. Lechermann, A. Georges, F. Jollet, T.O. Wehling, and A.I. Lichtenstein, Phys. Rev. B **77**, 205112 (2008)

[44] G. Rai, L. Crippa, D. Călugăru, H. Hu, F. Paoletti, L. de' Medici, A. Georges, B.A. Bernevig, R. Valentí, G. Sangiovanni, and T. Wehling, Phys. Rev. X **14**, 031045 (2024)

[45] S. Ryee, L. Klebl, G. Rai, A. Fischer, V. Crépel, L. Xian, A. Rubio, D.M. Kennes, R. Valentí, A.J. Millis, A. Georges, and T.O. Wehling, arXiv:2506.22325

[46] A. Fischer, L. Klebl, V. Crépel, S. Ryee, A. Rubio, L. Xian, T.O. Wehling, A. Georges, D.M. Kennes, and A.J. Millis, arXiv:2412.14296

[47] F. Wu, T. Lovorn, E. Tutuc, I. Martin, and A. MacDonald, Phys. Rev. Lett. **122**, 086402 (2019)

[48] T. Devakul, V. Crépel, Y. Zhang, and L. Fu, Nat. Commun. **12**, 6730 (2021)

[49] V. Crépel and A. Millis, Phys. Rev. Res. **6**, 033127 (2024)

[50] W.-X. Qiu, B. Li, X.-J. Luo, and F. Wu, Phys. Rev. X **13**, 041026 (2023)

[51] A. Fischer, L. Klebl, D.M. Kennes, and T.O. Wehling, arXiv:2407.02576

[52] D. Muñoz-Segovia, V. Crépel, R. Queiroz, and A.J. Millis, arXiv:2503.11763

[53] M.J. Calderón, A. Camjayi, A. Datta, and E. Bascones, arXiv:2412.20855

[54] H. Hu, G. Rai, L. Crippa, J. Herzog-Arbeitman, D. Călugăru, T. Wehling, G. Sangiovanni, R. Valentí, A.M. Tsvelik, and B.A. Bernevig, Phys. Rev. Lett. **131**, 166501 (2023)

[55] G.-D. Zhou, Y.-J. Wang, N. Tong, and Z.-D. Song, Phys. Rev. B **109**, 045419 (2024)

[56] Y.-J. Wang, G.-D. Zhou, S.-Y. Peng, B. Lian, and Z.-D. Song, Phys. Rev. Lett. **133**, 146001 (2024)

[57] D. Wong, K.P. Nuckolls, M. Oh, B. Lian, Y. Xie, S. Jeon, K. Watanabe, T. Taniguchi, B.A. Bernevig, and A. Yazdani, Nature **582**, 198 (2020)

[58] Y. Saito, F. Yang, J. Ge, X. Liu, T. Taniguchi, K. Watanabe, J.I.A. Li, E. Berg, and A.F. Young, Nature **592**, 220 (2021)

[59] A. Rozen, J.M. Park, U. Zondiner, Y. Cao, D. Rodan-Legrain, T. Taniguchi, K. Watanabe, Y. Oreg, A. Stern, E. Berg, P. Jarillo-Herrero, and S. Ilani, Nature **592**, 214 (2021)